Article

Investigating Electronic, Optical, Thermodynamic, and Thermoelectric Properties of SrO and SrO₂ Phases: A Density Functional Theory Approach

Hiren S. Patel, Vishnu A. Dabhi, and Aditya M. Vora*

Read Online

ACCESS | Metrics & More | Article Recommendations

ABSTRACT: The significance of strontium oxide (SrO) and strontium peroxide (SrO₂) is currently being investigated as one of the countless potential uses for green energy. However, few studies have examined the distinctive properties of several phases of SrO and SrO₂. In order to fill this research gap, we have conducted a study on their various properties through "density functional theory (DFT)" under ideal conditions. This includes the study of electronic, optical, thermodynamic, and thermoelectric properties of the above-mentioned materials. For this study, the "Quantum Espresso" tool in DFT using Perdew−Burke−Ernzerhof-generalized-gradient approximation (PBE-GGA) as the exchange−correlation functional and "Optimized Norm-Conserving Vanderbilt (ONCV)" as the pseudopotential has been used. The face-centered cubic (FCC), body-centered cubic (BCC), hexagonal-1, and hexagonal-2 phases of SrO and the tetragonal and orthorhombic phases of

SrO₂ have been selected for the aforesaid study, for which some structural information has already been available. During this study, the energy band gap as an electronic property; the dielectric constant, refractive index, absorption coefficient, reflectivity, and energy loss function as optical properties; entropy, heat capacity, Debye temperature, and Debye sound velocity as thermodynamic properties; and the Seebeck coefficient, thermal conductivity, electrical conductivity, and figure of merit as thermoelectric properties have been investigated. In addition, phonon dispersion curves and formation energies have been used to confirm the dynamical stability and thermodynamic stability, respectively, for all of the materials mentioned above. The curve showed that the FCC, hexagonal-1, and hexagonal-2 phases of "SrO" are dynamically stable. These materials have good optoelectronic properties and can be used in ultraviolet sensors due to their intermediate band gap and highest material response in the ultraviolet range. In terms of thermoelectric property, the maximum value of "figure of merit" for the above material has been achieved up to 0.5. Satisfactory agreement has been found between the current findings and the known theoretical and experimental findings.
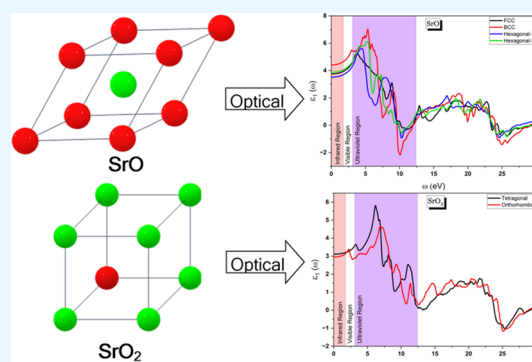
INTRODUCTION

Within the crust and subsurface of the earth, several phases of strontium oxide (SrO) and strontium peroxide (SrO₂) exist under various pressures and temperatures. SrO and SrO₂ are emerging as topics of interest for researchers due to their unique uses and characteristics. Due to the high refractivity and chemical stability of SrO and SrO₂, they are largely utilized in plasma displays, microelectronics, and television picture tubes to suppress X-ray radiation. According to a review of the literature, the majority of studies have focused solely on the electrical, structural, elastic, and thermoelectric properties of SrO cubic compounds, but less work has been done on the other phases of SrO$_x$ [x = 1, 2].[1−4] In this research, we have selected four phases of SrO (i.e., face-centered cubic (FCC), body-centered cubic (BCC), hexagonal-1, hexagonal-2) with space group ($F\bar{m}3m$, $P\bar{m}3m$, $P6_3mc$, $P6_3mmc$), respectively, and two phases of SrO₂ (tetragonal, orthorhombic) with space group ($I4mmm$, $Pnma$), respectively. We have computed the

electronic, optical, thermophysical, and thermoelectric properties of the aforementioned compounds.[5]

Face-centered cubic (FCC), commonly referred to as the "NaCl" structure, is the crystal structure of SrO at atmospheric pressure. Strontium cations (Sr²⁺) and oxide anions (O²⁻) are organized in this structure in a cubic lattice, with each cation being surrounded by six anions and the opposite being true (Figure 1a).[6] Up to a pressure of roughly 47 GPa, the FCC phase of SrO is stable; after that, it changes into a body-centered cubic (BCC) commonly referred to as the "CsCl" structure at high pressures.[7] A cubic lattice with O²⁻ atoms at
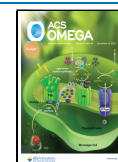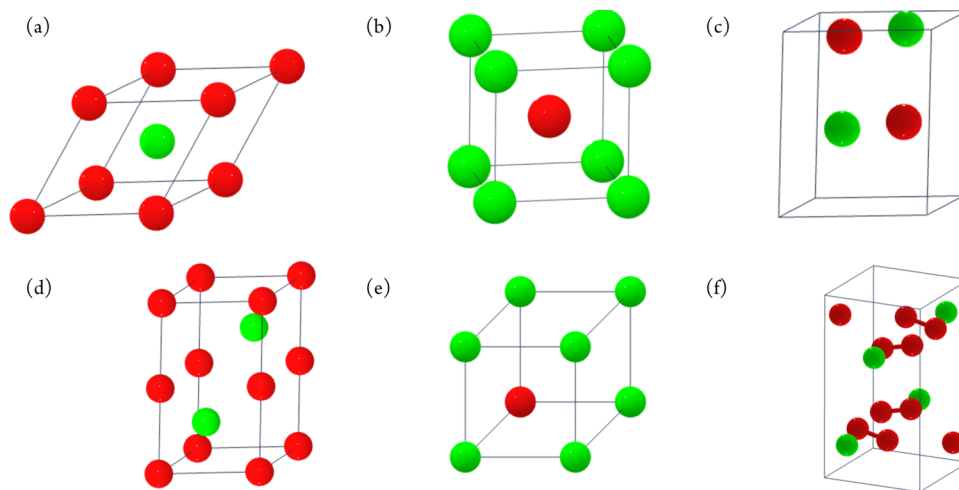
Figure 1. Atomic arrangements in the primitive cell of SrO phases including (a) face-centered cubic (FCC), (b) body-centered cubic (BCC), (c) hexagonal-1, and (d) hexagonal-2 and SrO_2 phases with (e) tetragonal and (f) orthorhombic structures, denoted by green spheres for "Sr" atoms and red spheres for "O" atoms, respectively.

the cube's corners and Sr^{2+} in its center defines the BCC structure (Figure 1b).[8,9] The increased packing density of the BCC phase makes it more stable under high pressures. At certain pressures and temperatures, SrO also occurs in hexagonal phases, with hexagonal-1 and hexagonal-2 being distinguished by their atomic arrangements. Atom Sr^{2+} in hexagonal-1 ($P6_3mmc$ space group) is electronically bonded to five equivalent O^{2-} atoms and forms a SrO_5 trigonal bipyramid with a range of Sr−O bond lengths between 2.47 and 2.58 Å (Figure 1c).[10] SrO (hexagonal-2) similarly crystallizes in the hexagonal $P6_3mmc$ space group, where Sr^{2+} is bounded by a 2.57 Å bond length to six equivalent O^{2-} atoms. Here, six equivalent Sr^{2+} atoms and O^{2-} are bound together to create OSr_6 octahedra (Figure 1d).[11,12]

SrO_2 exists in two phases in nature, one is the tetragonal phase and the other is the orthorhombic phase. The tetragonal phase is available at room temperature and is more stable than the orthorhombic phase and crystallizes in the "$I4mmm$" space group (Figure 1e).[5,13] While in the orthorhombic phase, SrO_2 crystallizes in the "$Pnma$" space group Figure 1f.[11,14]

As per the literature review, most of the work has been done only on FCC and BCC phases of SrO, and no work could be found in the case of hexagonal-1, hexagonal-2, and SrO_2 structures. Manal et al. investigated the structural, elastic, and electronic properties of strontium chalcogenide and examined the phase transition between the FCC (NaCl) and BCC (CsCl) phases of strontium oxide using density functional theory (DFT) within the generalized-gradient approximation (GGA).[15] Rajput et al. investigated the temperature-dependent transport properties of strontium chalcogenides in their rock salt and hexagonal monolayer phases using density functional theory. They also calculated the Seebeck coefficient, electrical conductivity, thermal conductivity, and figure of merit of these materials.[3] Hou et al. conducted research on electronic, structural, optical, and thermoelectric properties of strontium oxide at different pressures and concluded that FCC phase SrO is better thermoelectric material than BCC phase SrO.[2] Jacobson et al. experimentally reported the infrared dielectric response and lattice vibration of the strontium oxide's FCC phase.[16] Souadkia et al. studied the change in lattice dynamics and thermodynamic properties of SrO under various pressures.[17]

Wang et al. predicted a new monoclinic structure for strontium peroxide (SrO_2), which is energetically more favorable than the previously known tetragonal structure at ambient pressure and low temperature and reported a high-pressure phase of SrO_2 with $P2_1/c$ symmetries containing two layers of peroxide ions with different orientations at pressures higher than 36 GPa.[18] Cinthia et al. examined structural, electronic, and mechanical properties of alkaline earth metal oxides with cubic and hexagonal-1 phases using the VASP code.[4] Based on all of these factors and the currently available literature review, we have determined that there is room for further investigation into the different SrO_x [x = 1, 2] phases so that others may benefit from the knowledge gained from this research. In the future, the least known phases of SrO_x [x = 1, 2] may be synthesized in the lab under specific conditions by other researchers, and their results may be compared with the results of this work.

■ COMPUTATIONAL DETAILS

Here, using a first-principles approach and the density functional theory (DFT), a study has been carried out on SrO (FCC, BCC, hexagonal-1, hexagonal-2) and SrO_2 (tetragonal, orthorhombic).[19,20] DFT has been used to predict the aforementioned features for less well-known structures of SrO and SrO_2 since it is evident that DFT mimics experimental work with amazing precision.[21] All computations in the present study have been carried out using the Quantum Espresso package and the Thermo_pw tool.[22−24] In the literature analysis, it was found that most research works have incorporated ultrasoft and PAW as pseudopotentials with GGA functional for electron−electron and electron−ion interactions, while in this study, the scalar-relativistic optimized norm-conserving Vanderbilt (ONCV) pseudopotential is used along with the GGA approach, from SG15 database.[25−28] After several experiments with various materials, it has been proven that ONCV predicts the electrical and optical properties quite accurately but fails to calculate the p-DOS, as it only considers the valence electrons. Convergence tests of the plane-wave energy cutoff and the k-mesh grid have been carried out for all of the aforementioned phases of SrO_x [x = 1, 2] under the specific conditions, where the residual force is less than 10^{-3} Ry/Bohr and energy minimization must be under 10^{-4} Ry/

Table 1. Lattice Parameter(s) and Density of Various Phases of SrO and SrO$_2$ Compared with Available Data

compound	phase	present work		previously available data	
		lattice parameter (Å)	density (g/cm^3)	lattice parameter (Å)	density (g/cm^3)
SrO	FCC	a = 5.18	4.93	a = 5.17,[6] 5.18[3]	4.99[6]
	BCC	a = 3.13	5.59	a = 3.14,[2,8] 3.13[15]	5.55[2]
	hexagonal-1	a = 4.29, c = 5.18	4.26	a = 4.30, c = 5.16[4]	4.22[4]
				a = 4.04, c = 5.18[3]	
	hexagonal-2	a = 3.57, c = 6.23	4.98	a = 3.55, c = 6.22[12]	5.06[12]
SrO$_2$	tetragonal	a = 3.56, c = 6.82	4.59	a = 3.54, c = 6.68[5]	4.73[5]
				a = 3.56, c = 6.61[31]	
	orthorhombic	a = 4.50, b = 4.93, c = 8.50	4.23	a = 4.72, b = 4.95, c = 8.51[9]	

atom. After conducting convergence tests, a kinetic energy cutoff of 80 Ry and a k-mesh spacing of 0.15 Å^{-1} were initially selected for all calculations. However, for phonon calculations aimed at improving result accuracy, these parameters were subsequently adjusted to 120 Ry and 0.1 Å^{-1}, respectively.[29] With this configuration, vc-relax was performed on the aforementioned structures to find the lattice parameters and density that were appropriate with less than 0.01 Kbar stress, as given in Table 1. The results agree well with previous theoretical and experimental research. The CALYPSO (Crystal structure AnaLYsis by Particle Swarm Optimization) tool is used to validate and improve the structures of hexagonal SrO and orthorhombic SrO$_2$.[30] The constructions with the lowest energy and maximum stability factors were confirmed by CALYPSO.

Here, optical and thermoelectric properties of SrO$_x$ [x = 1, 2] have been calculated using estimated frequency-dependent complex dielectric function and semiclassical Boltzmann transport approximation, respectively.[32] For the calculation of thermoelectric transport properties for the aforementioned material, the BoltzTraP2 package has been used.[33] Vibrational energy, vibrational free energy, entropy, and specific heat of the system as thermodynamic properties have been calculated with the help of thermo_pw, a Quantum Espresso-assisted tool.[17] Furthermore, phonon dispersion curves have been plotted for all of the aforementioned structures, providing information regarding the dynamical stability.

RESULTS AND DISCUSSION

Electronic Band Structure Profile. The concept of the electronic band structure is essential in condensed matter physics, materials science, and electrical engineering. In materials, electrons have different energy levels that are grouped into bands. The band structure of a material determines its electrical and optical properties, making it important for many technological applications.

The electronic band structures of SrO$_x$ [x = 1, 2] have been visualized using optimized lattice parameters along the high symmetry points of the first Brillouin zone. The high symmetry directions in the first Brillouin zone for cubic SrO and hexagonal SrO are ($\Gamma - X - K - \Gamma$) and ($\Gamma - M - K - \Gamma$), respectively. For tetragonal and orthorhombic SrO$_2$, the high symmetry directions are ($\Gamma - M - S - \Gamma$) and ($\Gamma - X - S - Y - \Gamma$), respectively. As shown in Figure 2a, the valence band maximum (VBM) is observed at the high symmetry point "Γ" and the conduction band minimum (CBM) is observed at the high symmetry point "X" in the face-centered cubic (FCC) phase of SrO. This indicates that FCC-SrO has an indirect band gap. Whereas, in the body-centered cubic (BCC) phase of SrO, the VBM and the CBM are detected at the high

symmetry points 'M' and "Γ" respectively, as illustrated in Figure 2b. This demonstrates the indirect band-gap behavior of BCC-SrO. The hexagonal-1 and hexagonal-2 phases of SrO exhibit a direct band gap at the high symmetry point "Γ", as illustrated in Figure 2c,d. In the tetragonal phase of SrO$_2$, an indirect band gap can be observed along the high symmetry points "Γ" and 'M', which is shown in Figure 2e. The orthorhombic phase of SrO$_2$ also exhibits an indirect-band-gap semiconductor along the high symmetry points "X' and "Y", as per Figure 2f.[33] According to the electronic band structure profile, only hexagonal-1 and hexagonal-2 phases have a moderate and direct band gap. This makes them suitable for use in ultraviolet emission optoelectronic devices or LASER diodes, while other phases of SrO$_x$ [x = 1, 2] from Table 2 show moderate and indirect band gaps, suggesting that they can be used as ultraviolet sensors or absorbers. It is well known that semiconductors with medium energy band gaps are a diverse family of materials with numerous applications. As the need for more reliable and efficient electrical devices increases, they are becoming more and more important, and from the energy band-gap profile, we expect that "SrO" may be one of them.

From the literature review of previously conducted research, it can be said that most research on the electronic properties of SrO$_x$ [x = 1, 2] has focused on finding the electronic band gap. This is shown in Table 2, which also includes the results obtained in this study. These results suggest that the computational parameters used here are appropriate, so the same computational setup is continued for all further properties.

Optical Properties. The linear response in density functional theory (DFT) is used to determine the optical properties of materials. Here, we start with the ground-state density of the material and then introduce a modest electric field to perturb it, which represents the crucial quantity; here, the complex dielectric function $\varepsilon(\omega)$ depends on the frequency of light ω.[35]

$$\varepsilon(\omega) = \varepsilon_1(\omega) + i\varepsilon_2(\omega) \tag{1}$$

When defining a material's optical characteristics, both the real and imaginary parts of the dielectric function are significant. The imaginary part $\varepsilon_2(\omega)$ is related to the dissipation of electromagnetic waves in the material, whereas the real part $\varepsilon_1(\omega)$ is related to the polarization of the material. $\varepsilon_2(\omega)$ consists of two different components; the Drude formula can be used to characterize the first component of the imaginary dielectric constant of a material, which is caused by free-carrier absorption, and the second component, which is caused by interband transitions. The Drude formula describes how free electrons in a material absorb electromagnetic
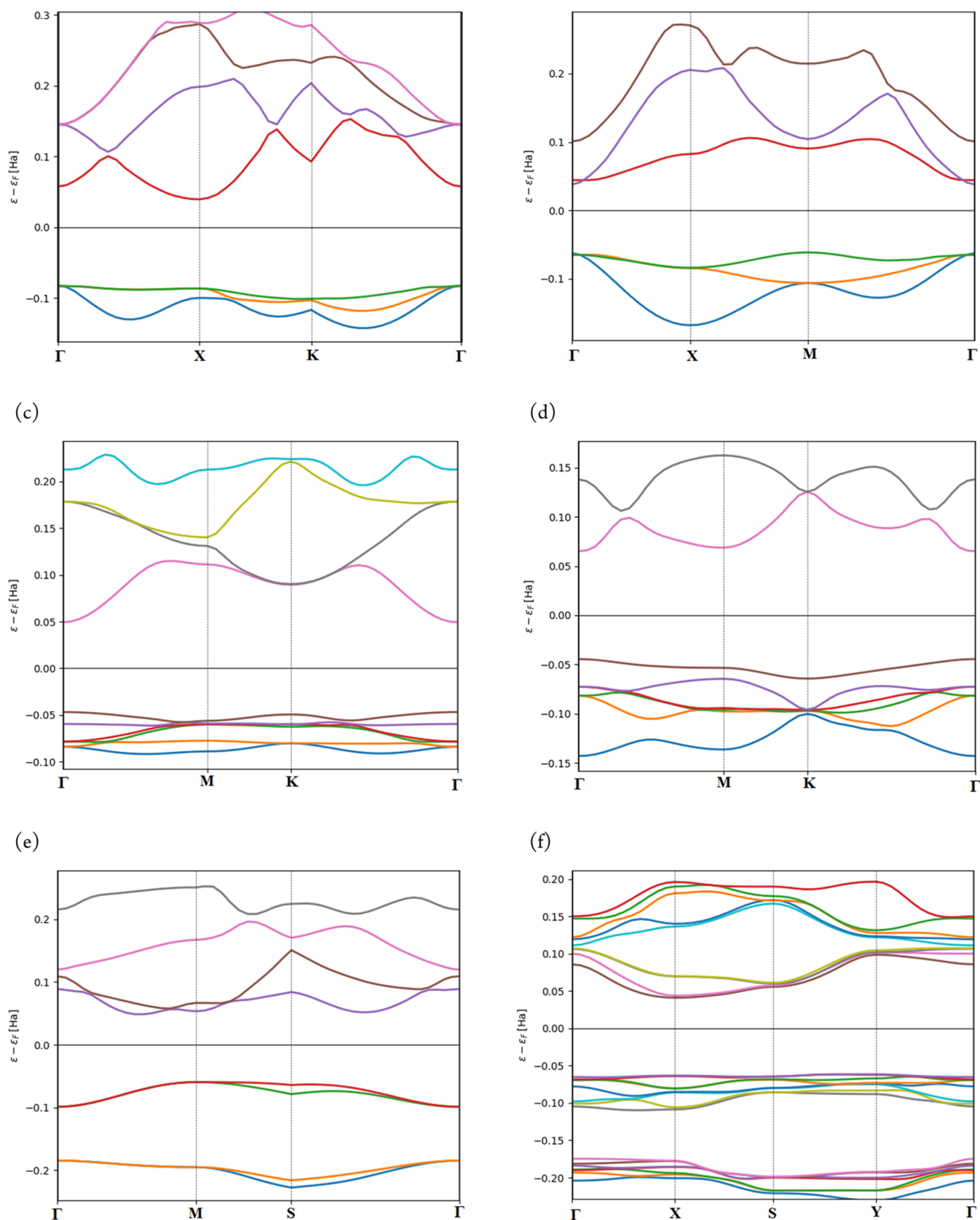
Figure 2. Electronic band structures of various SrO and SrO$_2$ phases: (a) FCC, (b) BCC, (c) hexagonal-1, and (d) hexagonal-2 for SrO phases and (e) tetragonal and (f) orthorhombic for SrO$_2$ phases. The zero-energy line represents the Fermi level, and energy values are provided in Hartree units (1 Ha = 27.21 eV).

Table 2. Energy Band-Gap Value for Various Phases of SrO and SrO$_2$ Compared with Available Data

compounds	phases	energy band gap (eV)	
		present Work	previously available data
SrO	FCC	3.30	3.33,[15] 3.20,[34] 3.27[3]
	BCC	2.27	2.27,[2] 2.74[8]
	hexagonal-1	2.62	2.68,[18] 2.56[10]
	hexagonal-2	3.05	2.94[12]
SrO$_2$	tetragonal	2.90	2.83,[18] 2.85[5]
	orthorhombic	2.72	2.78[5]

radiation. Due to free-carrier absorption, the imaginary fraction of the dielectric constant is inversely proportional to the frequency of the electromagnetic radiation. When an electron in an occupied state absorbs a photon with enough energy to cause it to jump to an unoccupied state in a higher energy band, this process is known as an interband transition. In contrast to the imaginary component caused by free-carrier absorption, the imaginary part of the dielectric constant caused by interband transitions is often significantly bigger. The

frequency of the electromagnetic radiation and the band structure of the material depend on how much each of the two components contributes to the imaginary dielectric constant. At low frequencies, free-carrier absorption makes up the majority of the contribution. The contribution from interband transitions becomes predominant at higher frequencies.[36]

$$\varepsilon_2(\omega) = \left\{ \frac{4\pi N_f e^2 \tau}{m^* \omega(1 + \omega^2 \tau^2)} \right\}$$
$$+ \left\{ \frac{8}{3\pi\omega^2} \sum_n \sum_{n'} \int_{BZ} |P_{nn'}(k)|^2 \frac{dS_k}{\nabla\omega_{nn'}(k)} \right\} \quad (2)$$

Here, N_f, m^*, τ, and $|P_{nn'}(k)|$ represent the number of free charges per unit volume, effective mass, relaxation time, and dipolar moment matrix, respectively.[37]

Effective mass can be calculated from the band structures of the materials using second-order quadratic fit,

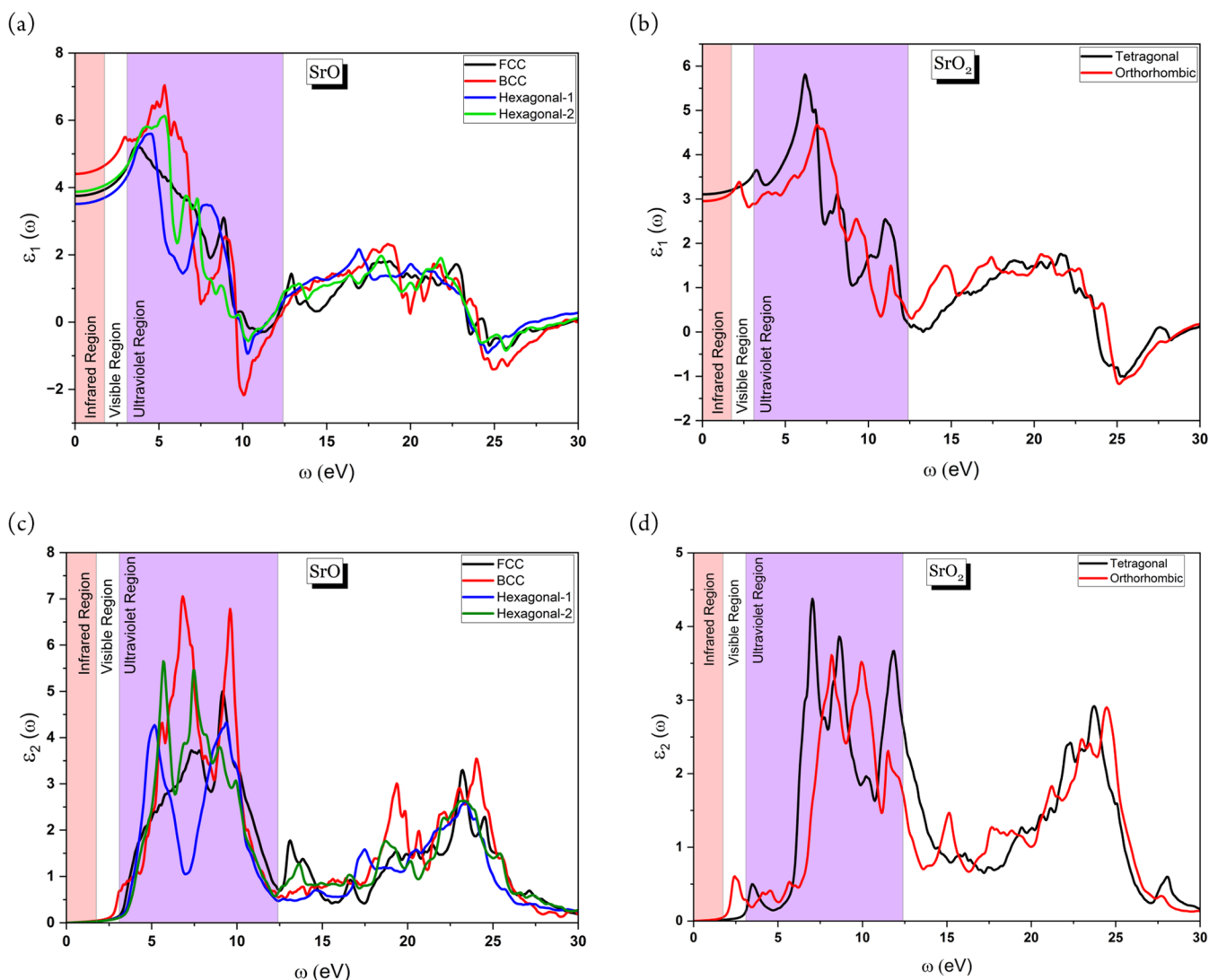$$m^* = \hbar^2 \left[\frac{\partial^2 E(k)}{\partial k^2} \right]^{-1} \quad (3)$$

Figure 3. Plot illustrating (a) real $\varepsilon_1(\omega)$ components of SrO, (b) real $\varepsilon_1(\omega)$ components of SrO$_2$, (c) imaginary $\varepsilon_2(\omega)$ components of SrO, and (d) imaginary $\varepsilon_2(\omega)$ components of the SrO$_2$ dielectric function as functions of electromagnetic radiation energy (ω) exclusively in the "xx" direction.

The imaginary dielectric constant $\varepsilon_2(\omega)$ is an indicator of a material's dielectric losses. The dielectric losses increase with increasing imaginary dielectric constant. Dielectric losses can cause electromagnetic radiation to heat up, absorb, and scatter.

Using the aforementioned relationships, the real portion of $\varepsilon_1(\omega)$ could be approximated as follows using the Kramer–Kroing relation[38]

$$\varepsilon_1(\omega) = 1 + \frac{2}{\pi}P \int_0^\infty \frac{\omega' \varepsilon_2(\omega')}{\omega'^2 - \omega^2} d\omega' \qquad (4)$$

The real part of the dielectric function $\varepsilon_1(\omega)$ explains the polarizing behavior of the material. The static dielectric constant, $\varepsilon_1(0)$, can be observed in Figure 3a,b at $\omega = 0$ and is also listed in Table 3 for the aforementioned materials. The

Table 3. Comparison of Static Dielectric Constants $\varepsilon_1(0)$ with Previously Reported Data

compound	phase	static dielectric constant	
		present work	previously available data
SrO	FCC	3.75	3.77,[39] 3.46,[16] 3.78[40]
	BCC	4.40	4.65[17]
	hexagonal-1	3.51	3.47[41]
	hexagonal-2	3.88	
SrO$_2$	tetragonal	3.11	
	orthorhombic	2.95	

first observable peaks of the real part of dielectric constant $\varepsilon_1(\omega)$ for all SrO phases are located in the ultraviolet region between 3 and 5 eV, while the peak values for the tetragonal and orthorhombic phases of SrO$_2$ are between 6.5 and 7.5 eV. These peaks form due to the direct transition of electrons from VB to CB, which gradually declines after the sudden increase. Negative values of the dielectric constant at a particular range of energy cause poor optical losses, reflectance, and transmission.

The imaginary part of the dielectric constant $\varepsilon_2(0)$ is zero in Figure 3c,d, which indicates that SrO_x [$x = 1, 2$] are pure semiconductor materials with no energy dissipation. The first peak in the spectrum occurs between 2.5 and 3.5 eV, as shown in Figure 3c,d, which is consistent with the energy band-gap

values of the aforesaid materials. Here, the first peaks of the spectra for said materials are located in the ultraviolet region. The maximum values of $\varepsilon_2(\omega)$ occur at 7.50, 6.81, 5.22, 5.73, 7.09, and 8.23 eV for FCC, BCC, hexagonal-1, hexagonal-2, tetragonal, and orthorhombic SrO_x [$x = 1, 2$], respectively. Following that, it is possible to see a drop in the spectra of SrO_x [$x = 1, 2$] as the energy level increases. Numerous other optical parameters, including the dielectric loss $L_0(\omega)$, refractive index $\eta(\omega)$, extinction coefficient $k(\omega)$, reflectivity $R(\omega)$, and absorption coefficient $\alpha(\lambda)$, can be determined using the dielectric functions.

The energy loss function is a key concept in the study of optical properties because it helps us understand how materials behave and react to light. The imaginary portion of the inverse dielectric function $\varepsilon(\omega)$ is used to calculate the energy loss function. It describes the relationship between incident photon energy and the energy a substance absorbs or loses.

$$L_0(\omega) = \text{Im}\left(-\frac{1}{\varepsilon(\omega)}\right) \qquad (5)$$

The electron energy-loss spectroscopy (EELS) and the inelastic scattering of electrons in a material are both intimately related to the energy loss function. It offers important knowledge on the collective electronic excitations, or plasmons, as well as other electronic transitions that take place within the substance.[35] The first peak in the energy loss spectrum has been observed in the far-ultraviolet region, and a significant loss was found between 25 and 30 eV for all phases of SrO_x [$x = 1, 2$] (Figure 4).

The refractive index $\eta(\omega)$ contains details about how light behaves in the substance. It is known that the speed of light in a substance is inversely proportional to the refractive index of that substance. The refractive index also determines the bending or dispersion of light in the substance. According to Figure 5a,b, the refractive index has a high value in the near-ultraviolet region but then declines significantly in the high-energy region, ultimately dropping below the free space refractive index value in that region. As per the following equation, the refractive index $\eta(\omega)$ is obtained using the real and imaginary parts of the dielectric function.
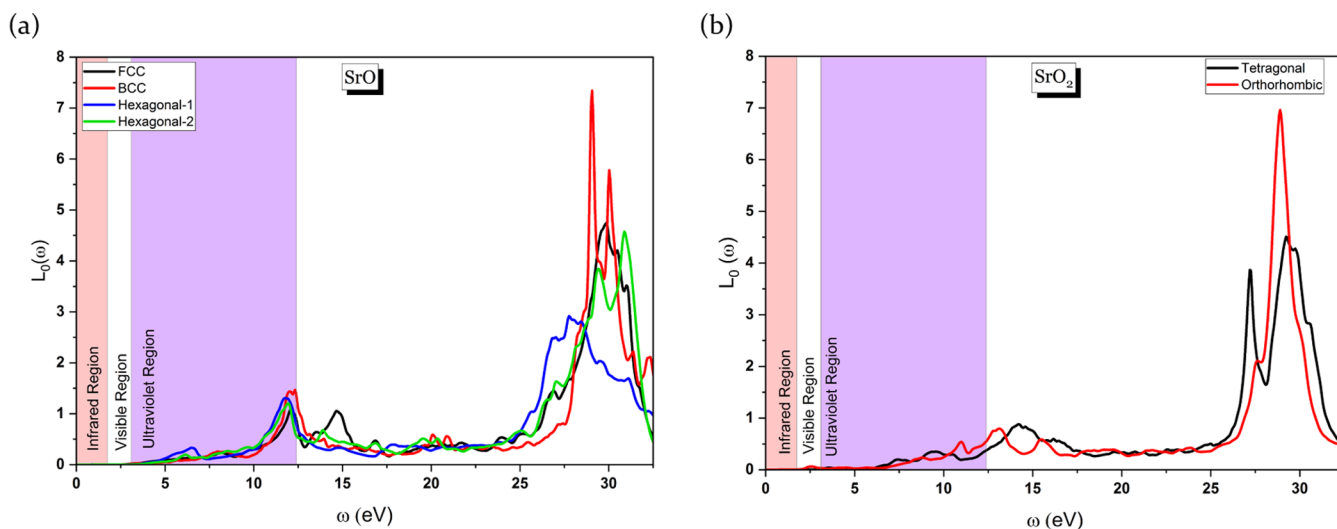
(a)

(b)

Figure 4. Energy loss profiles of (a) SrO and (b) SrO$_2$ as a function of incident photon energy: Graphical representation.
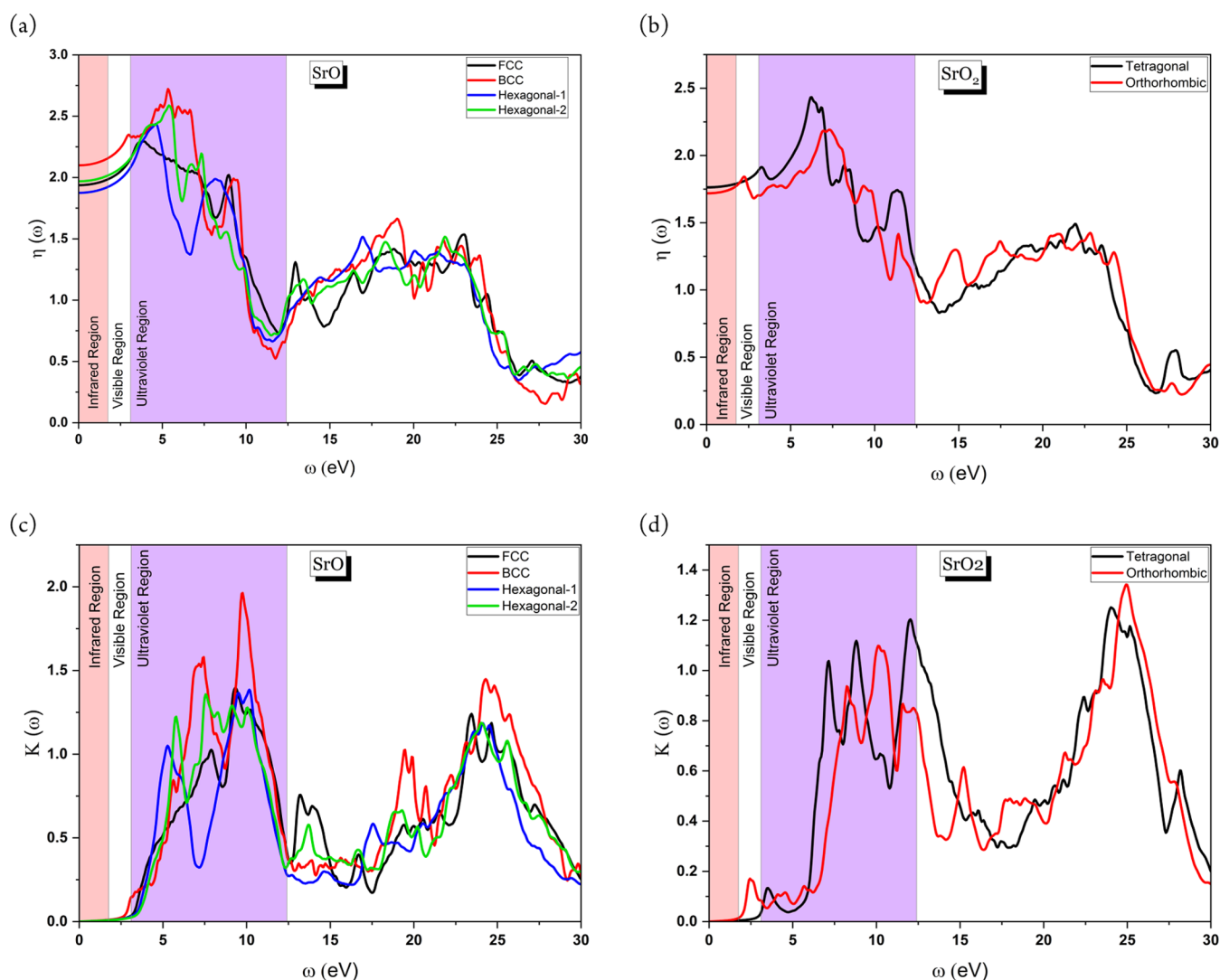
Figure 5. Refractive indices (η) for (a) SrO and (b) SrO$_2$ and extinction coefficients (K) for (c) SrO and (d) SrO$_2$ as functions of photon energy (ω).

Table 4. Static Refractive Index and Refractivity for All Phases of SrO and SrO$_2$

compound	phase	static refractive index		reflectivity	
		present work	previously available data	present work	previously available data
SrO	FCC	1.93	1.92,[44] 1.94[39]	0.110	0.090[45]
	BCC	2.10	-	0.137	-
	hexagonal-1	1.87	-	0.100	-
	hexagonal-2	1.97	-	0.115	-
SrO$_2$	tetragonal	1.76	-	0.08	-
	orthorhombic	1.72	-	0.08	-

$$\eta(\omega) = \left[\frac{\sqrt{\varepsilon_1^2(\omega) + \varepsilon_2^2(\omega)} + \varepsilon_1(\omega)}{2} \right]^{1/2} \quad (6)$$

For $\omega = 0$, the value of the refractive index $\eta(\omega)$ is known as the static refractive index $\eta(0)$ for the substance. We have derived the values of the static refractive index from Figure 5a,b and listed them in Table 4. The static refractive index $\eta(0)$ can also be calculated using the Penn's relation.[42]

$$\eta(0) = \sqrt{\varepsilon_1(0)} \quad (7)$$

The extinction coefficient $k(\omega)$ is the imaginary part of the complex refractive index function, $N(\omega) = \eta(\omega) + ik(\omega)$, and it is derived by the Kramer–Kroing relation.[38]

$$k(\omega) = \left[\frac{\sqrt{\varepsilon_1^2(\omega) + \varepsilon_2^2(\omega)} - \varepsilon_1(\omega)}{2} \right]^{1/2} \quad (8)$$

The extinction coefficient $k(\omega)$, also known as the attenuation coefficient, is related to the absorption of light in a material at a given photon energy ω. The value of $k(\omega)$ is zero at $\omega = 0$, and it thresholds at a certain photon energy
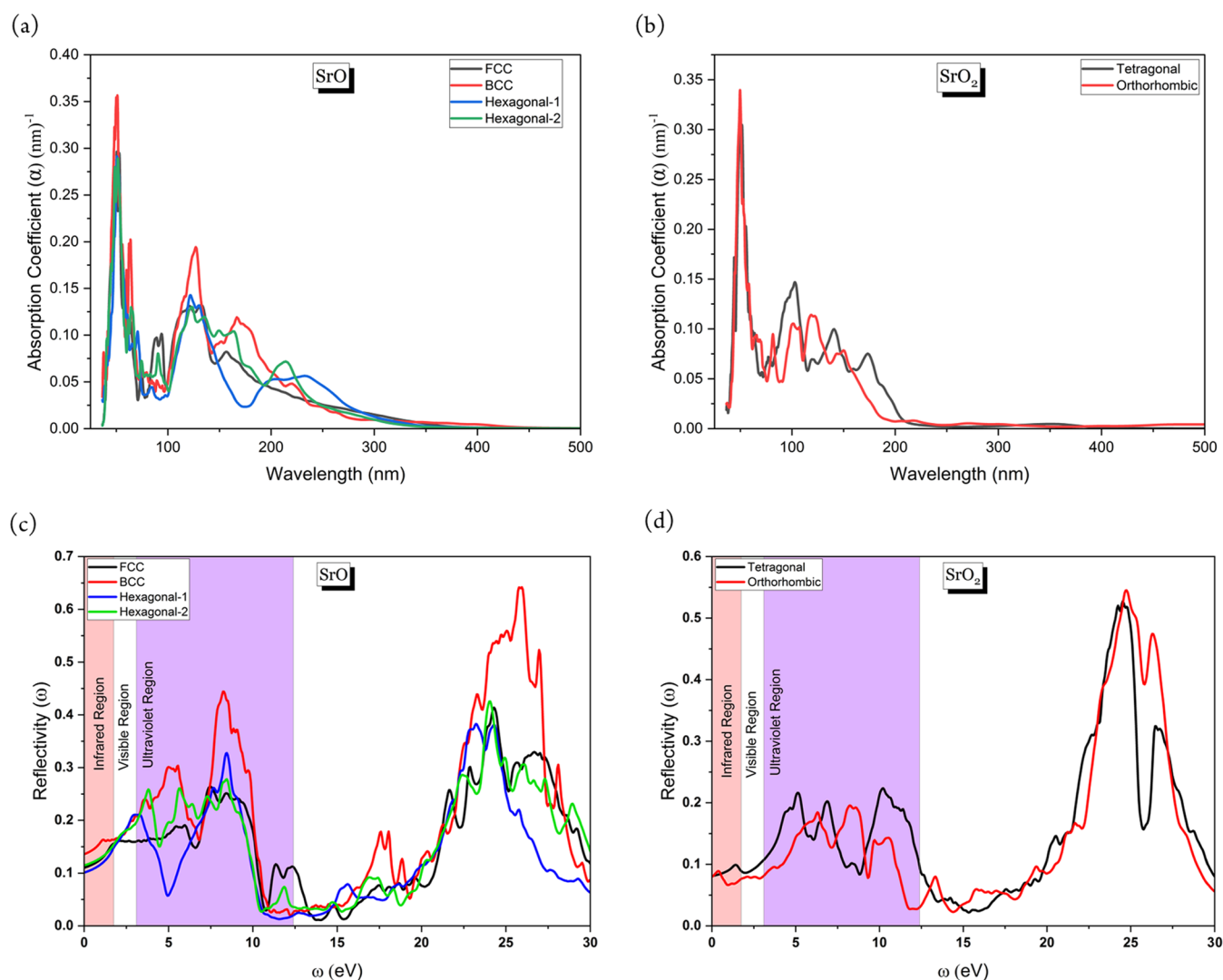
Figure 6. Graph depicting the absorption coefficient (α) as a function of the wavelength for (a) SrO and (b) SrO$_2$ and reflectivity in relation to photon energy (ω) for (c) SrO and (d) SrO$_2$.

whose value is related to the optical energy gap of the material.[43] The threshold value for all SrO phases lies between 2.55 and 3.05 eV, while for the phases of SrO$_2$, it is between 1.95 and 3.05 eV (Figure 5). For the SrO$_x$ [x = 1, 2] phases, all of the observable peaks lie in the near-ultraviolet region and gradually decline in the far-ultraviolet region.

The amount of light absorbed by a substance is determined by its absorption coefficient. The absorption coefficient is significant in photovoltaic cells because it affects how much of the solar spectrum is converted into electrical energy. Electrons can be excited from the valence band (VB) to the conduction band (CB) when light is absorbed by a substance. This operation requires a certain amount of energy corresponding to the band-gap energy of the material. The probability of this process occurring is measured by the absorption coefficient $\alpha(\lambda)$.

$$\alpha(\lambda) = \frac{4\pi k}{\lambda} \quad (9)$$

The first significant absorption peak lies at ∼50 nm (UV−C) for all SrO$_x$ [x = 1, 2] phases (Figure 6a,b), indicating that they have good electromagnetic radiation absorption capacity.

The percentage of incident light that is reflected back from a material's surface is known as reflectivity. It can be stated as follows in terms of the refractive index and the extinction coefficient.

$$R(\omega) = \frac{(\eta - 1)^2 + k^2}{(\eta + 1)^2 + k^2} \quad (10)$$

As shown in Figure 6c,d, the value of static reflectivity at ω = 0 can be easily obtained; the reflectivity is noted to be significantly lower in the visible and near-ultraviolet region, while its value appears to be greater than 50% for high-frequency photons. As shown in Figure 6c,d, most values for static reflectivity are reported to be around 10% of the incident light (Table 4), indicating that SrO could be used as good photovoltaic devices. According to Table 4, the FCC phase of SrO has a good agreement with the already available data, while for the other phases, this is the first trial to investigate the optical properties, and, therefore, their data are not available so far.

Thermodynamic Properties. A set of physical parameters known as the thermodynamic properties of a material define the energy, entropy, and other thermal properties of the
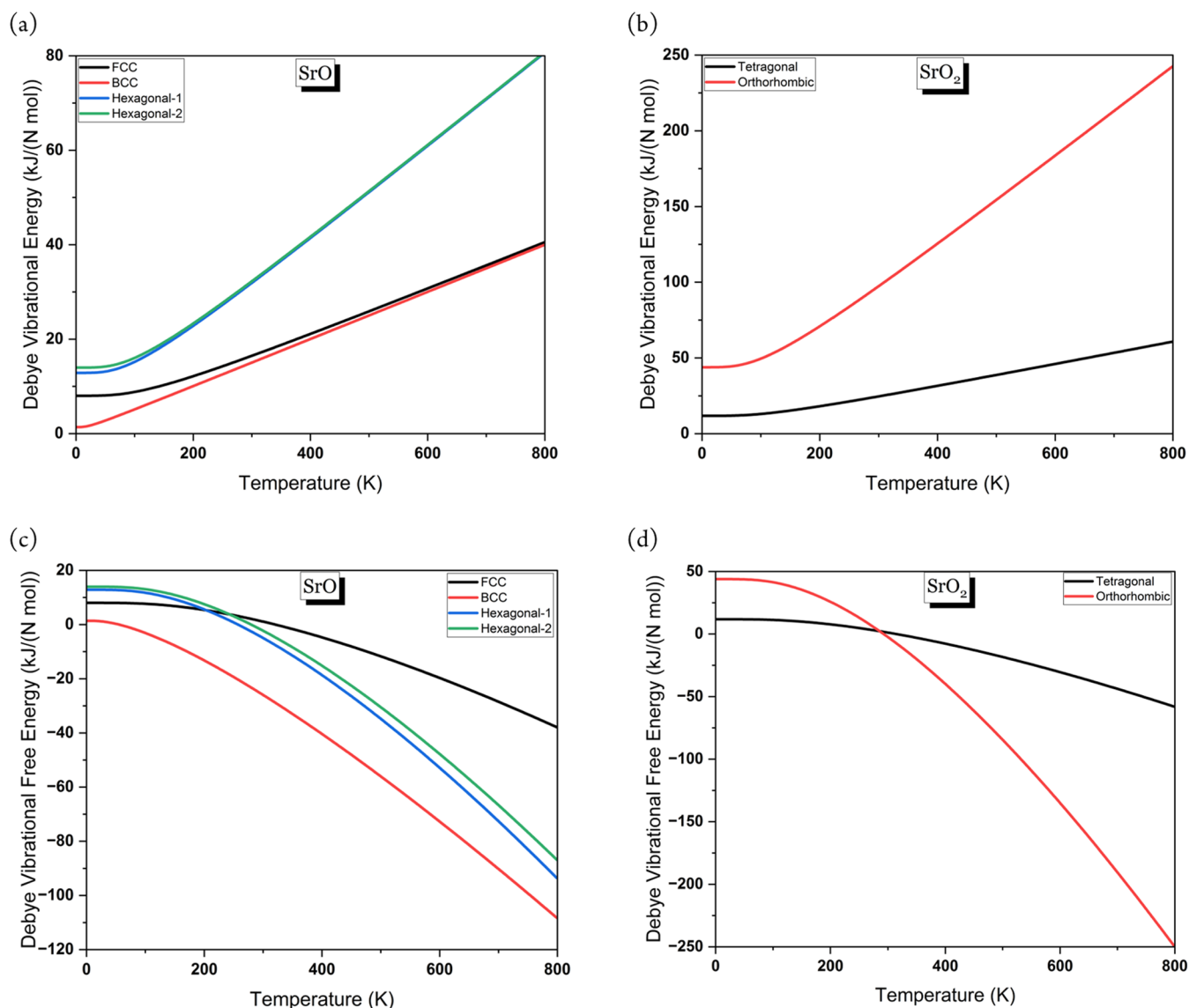
Figure 7. Temperature-dependent profiles of Debye vibrational energy for different phases of (a) SrO and (b) SrO$_2$ and free energy for different phases of (c) SrO and (d) SrO$_2$.

material. Knowledge of these properties is essential to understanding the behavior of materials under various conditions such as temperature, pressure, and composition. In DFT, the thermodynamic properties can be evaluated from the quasi-harmonic Debye model, in which the lattice vibrations are used to calculate the modes of the harmonic oscillator.[46,47] The thermodynamic properties have been calculated using "Quantum Espresso" and "Thermo_pw" tool.[23]

The vibrational energy of the lattice at absolute zero temperature is known as the Debye vibrational energy, also known as the energy of the highest-frequency vibration in the material, from which we can determine the strength of the intermolecular bonds in the material. It is said that the higher the Debye vibration energy, the stronger the interactions between the molecules of the solid and the harder the solid. The melting point of a material depends on its Debye vibrational energy such that the higher the Debye vibrational energy, the higher the melting point. According to CIF, N, which stands for the number of formula units per cell in Figure

7, has a value of 1 for cubic phases, 2 for hexagonal and tetragonal phases, and 4 for orthorhombic phases. Thus, we may obtain the right picture by dividing all of the values in Figure 7 by N. According to the description above, it is clear that in Figure 7a,b, the cubic phases of SrO exhibit more interatomic interactions than the hexagonal phases of SrO, and the tetragonal phase of SrO$_2$ exhibits more interatomic forces than the orthorhombic phase. This makes it obvious that the cubic and tetragonal phases of SrO$_x$ [x = 1, 2] can have melting points that are greater than the hexagonal and orthorhombic phases, respectively.

The thermal energy produced by the vibrating atoms in the crystal is known as the Debye free vibrational energy, which is related to the stability of the material. It is important because we can use it to calculate the specific heat of a crystal as well as other thermodynamic characteristics such as thermal expansion and thermal conductivity. From Figure 7c,d and the factors discussed above, it is clear that the SrO FCC and SrO$_2$ tetragonal phases are more stable than the other phases up to the normal temperature range.
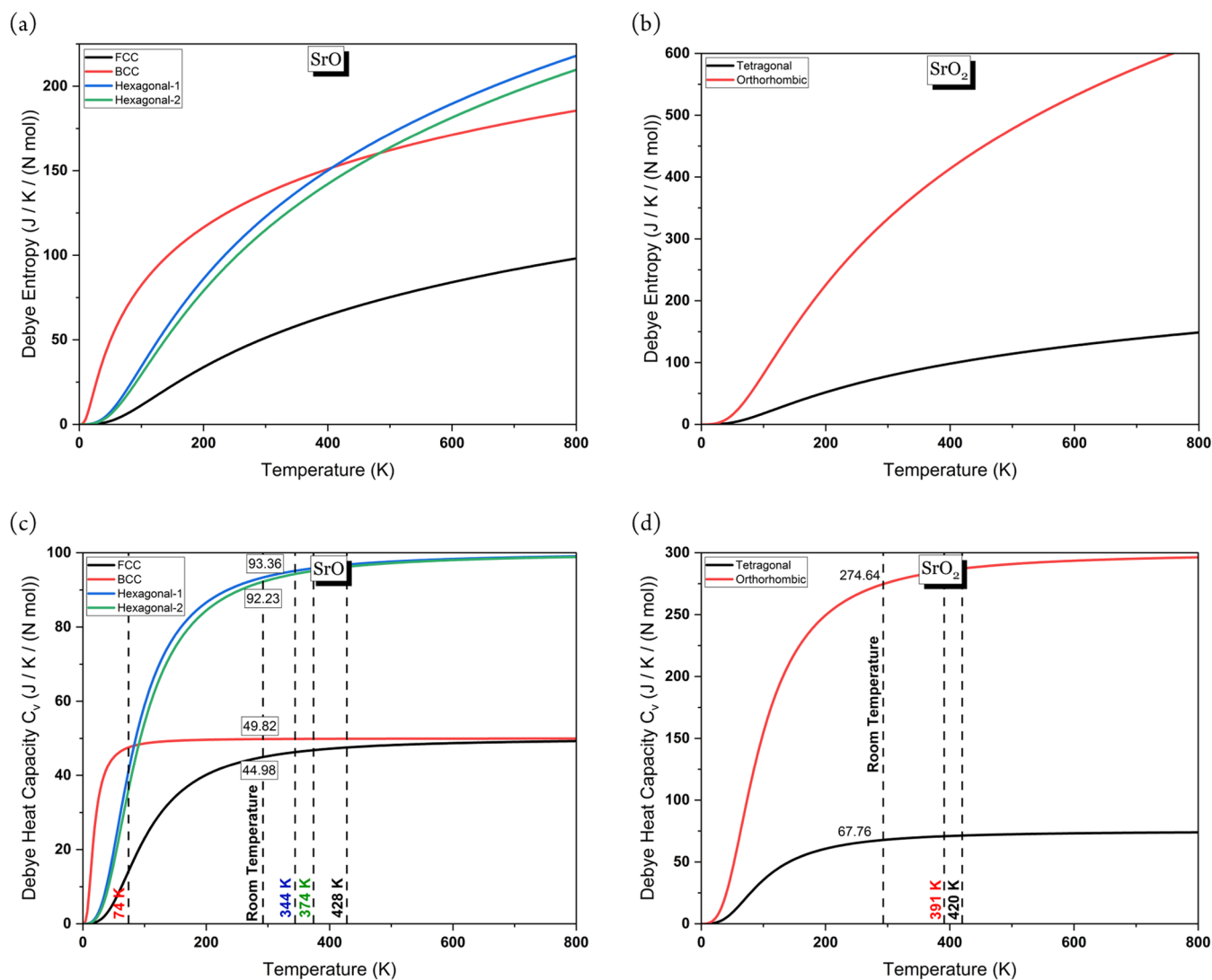
Figure 8. Illustration of the temperature-dependent profiles of Debye entropy (S) for various phases of (a) SrO and (b) SrO$_2$ and Debye heat capacity (C_v) for various phases of (c) SrO and (d) SrO$_2$. In panels (c) and (d), the heat capacity values at room temperature for various phases are highlighted within boxes, while dotted lines represent the corresponding Debye temperatures for these phases, color-coded for clarity.

Table 5. Entropy (S) and Heat Capacity (C_v) Values at Room Temperature, along with Debye Temperature (θ_D) for Different Phases of SrO and SrO$_2$

compound	phase	entropy (J Nmol/K)		C_v (J Nmol/K)		θ_D (K)	
		present work	other work	present work	other work	present work	other work
SrO	FCC	51.40	50.19[39]	44.98	44.95[39]	428	430[4]
			55.80[48]		46.70[46]		438[39]
			52.70[46]		45.01[49]		446[50]
	BCC	136.82		49.82		74	
	hexagonal-1	123.13		92.23		344	
	hexagonal-2	115.35		93.36		374	
SrO$_2$	tetragonal	78.49		67.76		420	
	orthorhombic	333.58		274.64		391	

The Debye model suggests that a solid's lattice vibrations can be considered a group of independent harmonic oscillators. However, in practice, there is some systemic disturbance, and the lattice vibrations are not completely independent. The entropy term in the Debye model explains this disorder. As the vibrations get more disordered with temperature, the entropy term in the Debye model increases.

This is due to the fact that as temperature increases, atoms gain energy and have more ability to vibrate beyond their equilibrium positions. The entropy of the FCC phase of strontium and the tetragonal phase of strontium is shown in Figure 8a,b to be relatively low, which further supports the excellent stability of the materials.
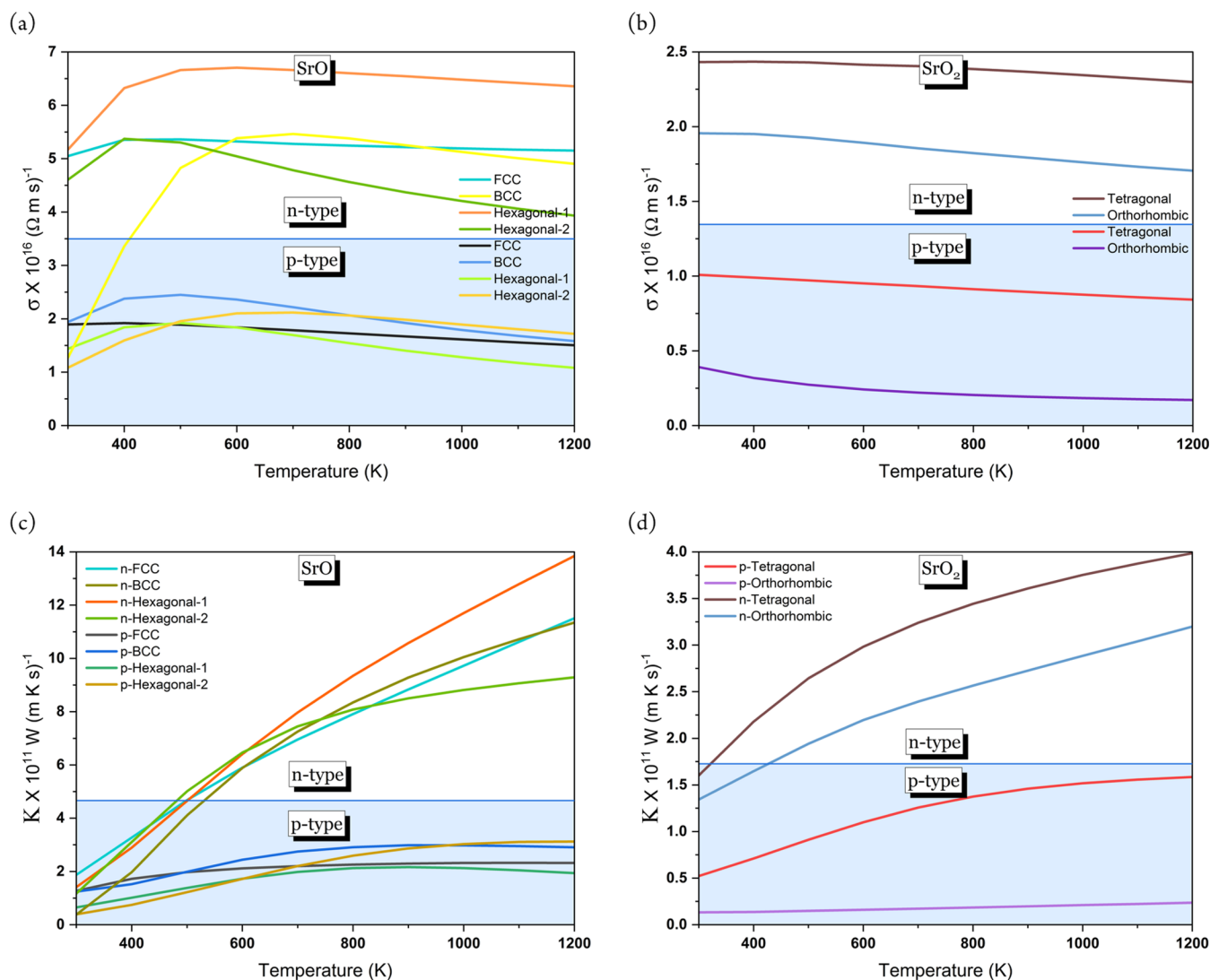
Figure 9. Graph illustrating the temperature-dependent electrical conductivities (σ/τ) for various phases of (a) SrO and (b) SrO$_2$ and thermal conductivities (κ/τ) for various phases of (c) SrO and (d) SrO$_2$ with charge carrier concentrations ($\pm 10^{16}$ cm^{-3}) and $\tau = 10$ fs.

C_v is the heat capacity at constant volume in the Debye model. It represents the amount of energy needed to increase a solid's temperature while maintaining a constant volume. The Debye model implies that a solid's lattice vibrations can be viewed as a group of separate harmonic oscillators. This indicates that each oscillator's energy is quantized and can only have discrete values. The heat capacity in the Debye model is proportional to T^3 at low temperatures. This is such that only the low-frequency lattice vibrations are excited when the temperature is low. The heat capacity increases as the temperature increases as more and more lattice vibrations become stimulated. The Debye model's heat capacity approaches a constant value at high temperatures. This is due to the fact that at high temperatures, all lattice vibrations are stimulated, and the heat capacity is constrained by the solid's degree of freedom. Heat capacity at room temperature and Debye temperature values are depicted in Figure 8c,d and listed in Table 5.

A solid's lattice vibrations' stiffness is measured by the Debye temperature. The lattice vibrations get stiffer and have a greater heat capacity at constant volume as the Debye temperature increases.

According to Table 5, the FCC phase of SrO has a good agreement with the already available data, while for the other phases, this is the first trial to investigate the thermodynamic properties, and therefore their data are not available so far.

Thermoelectric Properties. Nowadays, the world is trying to reduce its dependence on conventional sources of energy and find more efficient as well as sustainable ways to use energy, thus increasing the demand for thermoelectric materials. In this effort, thermoelectric materials have the potential to be very important, so work is ongoing to develop new and better materials. Thermoelectric materials have the ability to generate electricity from waste heat, are used to make Peltier coolers for electronic devices, are used in spacecraft applications to generate electricity and regulate temperature, or are used in medical devices to generate heat or cold for therapeutic purposes.[51]

For all SrO$_x$ [$x = 1, 2$] phases, the thermoelectric properties have been evaluated using the semiclassical Boltzmann transport theory and the rigid band method, as implemented in the BoltzTraP algorithm.[33] According to theory, the maximum possible efficiency of a thermoelectric material depends on the hot-end temperature T_h, the cold-end
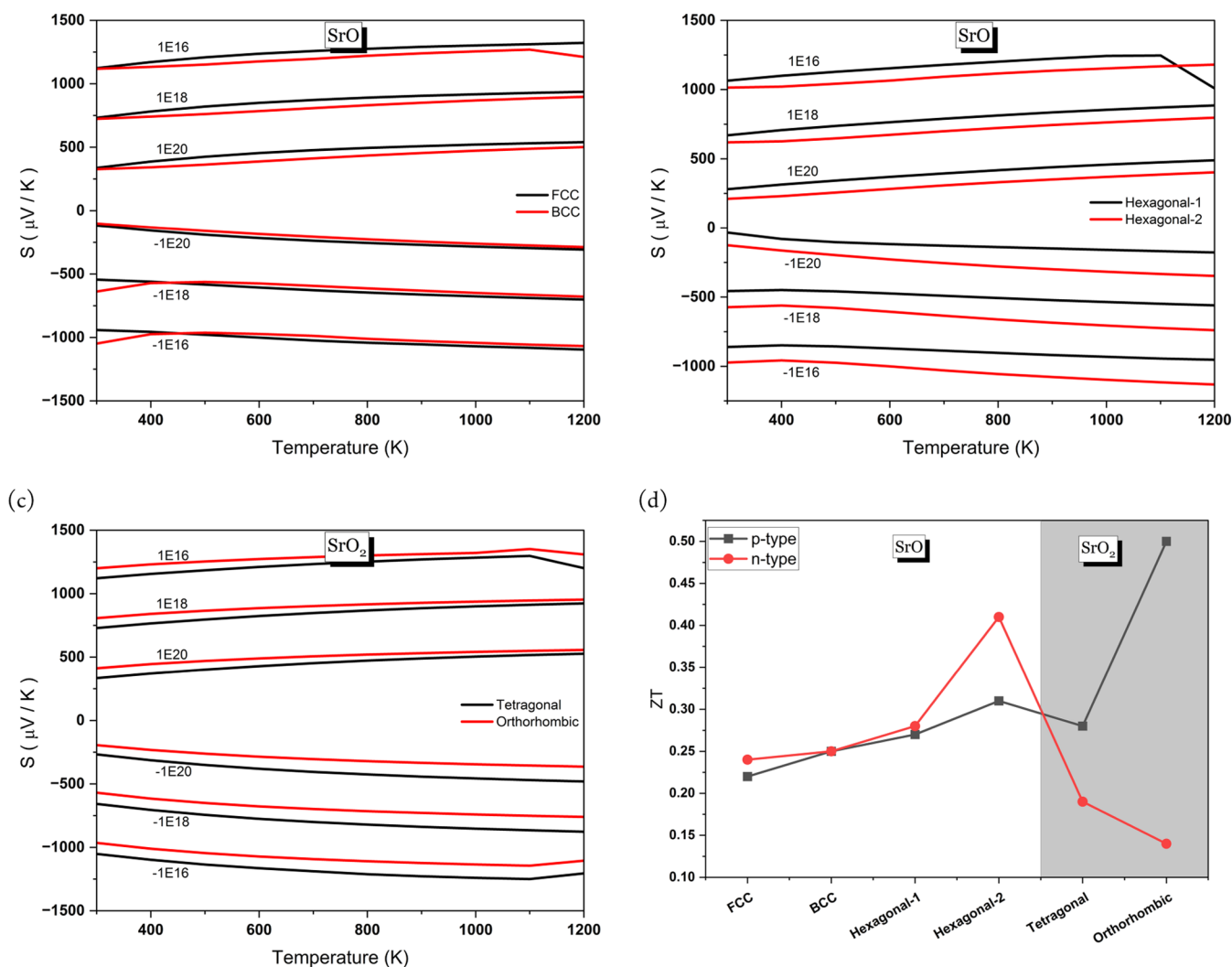
Figure 10. Graph depicting the Seebeck coefficient as a function of temperature for (a) cubic phases of SrO, (b) hexagonal phases of SrO and (c) SrO$_2$, and the figure of merit for different phases of (d) SrO and SrO$_2$, considering both n-type and p-type charge carrier concentrations.

temperature T_c, and ZT_e of the material, which is expressed by the following equation.[52]

$$\eta_{max} = \frac{T_h - T_c}{T_h} \times \frac{\sqrt{1 + ZT} - 1}{\sqrt{1 + ZT} + \frac{T_c}{T_h}} \qquad (11)$$

Here, $T = \frac{(T_h + T_c)}{2}$ and ZT_e is a dimensionless quantity, also referred to as the figure of merit of the material,[53] where ZT depends on thermoelectric power (Seebeck's coefficient) S, and electrical conductivity σ and total thermal conductivity $\kappa = \kappa_e + \kappa_l$ (κ_e= electronic thermal conductivity and κ_l = lattice thermal conductivity, for low carrier concentration, $\kappa_l \gg \kappa_e$, so $\kappa \approx \kappa_l$ and vice versa), are also expressed by the following equation,

$$ZT = \frac{S^2 \sigma}{\kappa} T \qquad (12)$$

For the maximum value of the figure of merit,

$$ZT_e = \frac{S^2 \sigma}{\kappa_e} T \qquad (13)$$

In BoltzTrap, the transport distribution function is denoted by the following equation, where, v_α, v_β, and τ_k are group velocities and relaxation time (average value of τ is taken as 10^{-14} s) of the charge carrier.[54]

$$\Xi_{i,k} = \sum_{i,k} v_\alpha v_\beta \tau_k \qquad (14)$$

The electrical conductivity (σ), thermal conductivity (κ), and the Seebeck coefficient (S) can be expressed as a function of temperature (T), electron contribution (ε), and also the chemical potential (μ), as given by the following equations (value of ε varies between $\mu - k_B T$ and $\mu + k_B T$).[55]

$$\sigma = e^2 \int \Xi_{i,k} \left[-\frac{\partial F_0(T, \varepsilon, \mu)}{\partial \varepsilon} \right] d\varepsilon \qquad (15)$$

$$k = \frac{e k_B}{\sigma} \int \Xi_{i,k} \left(\frac{\varepsilon - \mu}{k_B T} \right) \left[-\frac{\partial F_0(T, \varepsilon, \mu)}{\partial \varepsilon} \right] d\varepsilon \qquad (16)$$

$$S = k_B^2 T \int \Xi_{i,k} \left(\frac{\varepsilon - \mu}{k_B T} \right)^2 \left[-\frac{\partial F_0(T, \varepsilon, \mu)}{\partial \varepsilon} \right] d\varepsilon \qquad (17)$$

Table 6. Thermoelectric Properties of SrO and SrO$_2$ at a 300 K Temperature: The Seebeck Coefficient, Electrical Conductivity (σ/τ), Thermal Conductivity (κ/τ), and Maximum Figure of Merit for $\pm 10^{16}$ cm^{-3} Charge Carrier Concentrations

compound	phase	S (μV/K)		(σ/τ) $\times 10^{16}$ (Ω ms)$^{-1}$		(κ/τ) $\times 10^{11}$ W(m Ks)$^{-1}$		ZT_e	
		P	N	P	n	p	n	p	n
SrO	FCC	1118.3	940.8	1.89	5.05	1.28	1.88	0.22	0.24
	BCC	1118.3	1047.8	1.94	1.27	1.25	0.38	0.25	0.25
	hexagonal-1	1064.5	860.1	1.43	5.17	0.65	1.41	0.27	0.28
	hexagonal-2	1014.4	972.9	1.09	4.61	0.39	1.17	0.31	0.41
SrO$_2$	tetragonal	1122.1	1051.4	1.01	2.43	0.53	1.60	0.28	0.19
	orthorhombic	1200.9	964.0	0.40	1.96	0.13	1.34	0.50	0.14
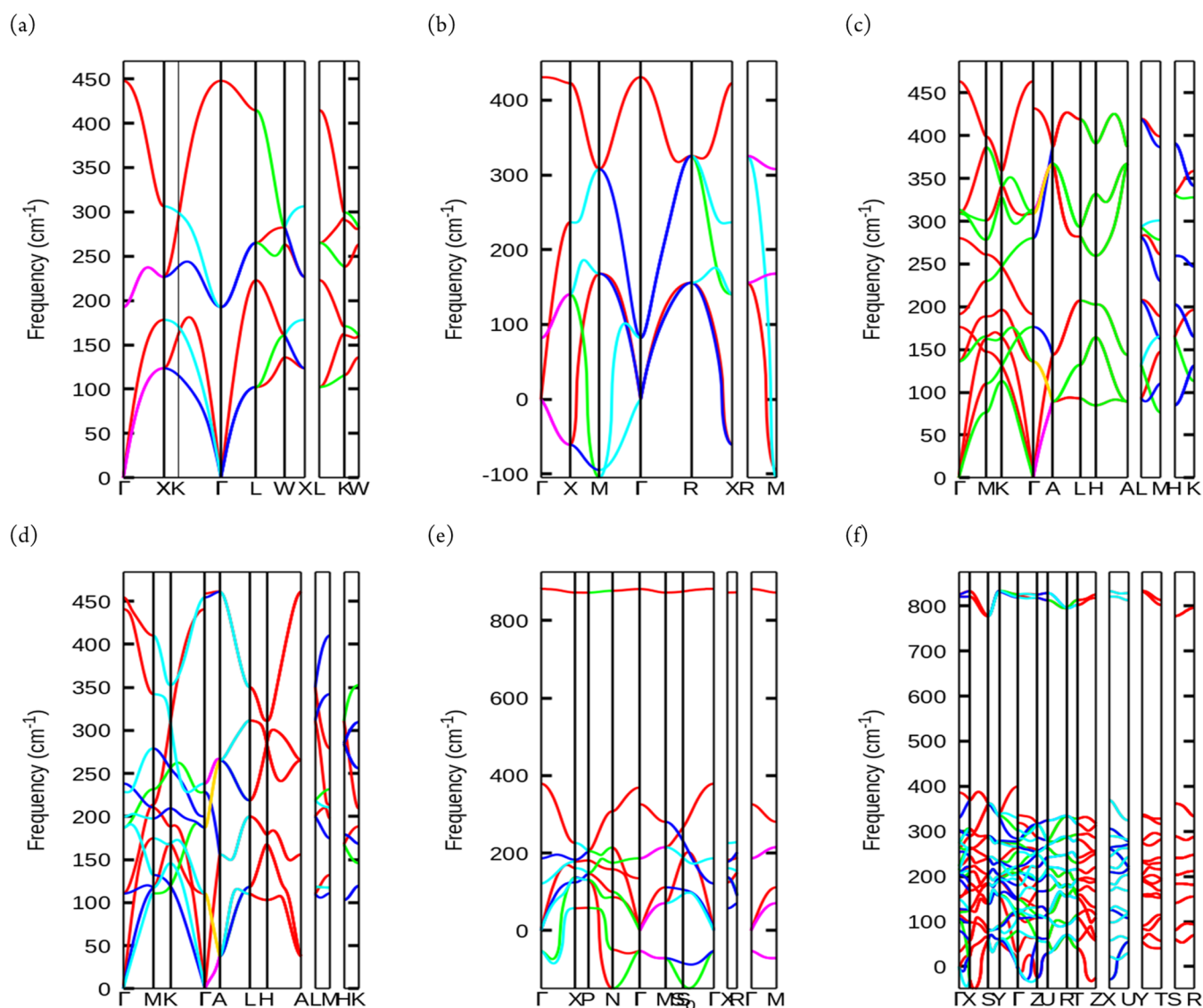
Figure 11. Phonon dispersion curves of SrO and SrO$_2$ in different structural phases: (a) FCC phase SrO, (b) BCC phase SrO, (c) hexagonal-1 phase SrO, (d) hexagonal-2 phase SrO, (e) tetragonal phase SrO$_2$, and (f) orthorhombic phase SrO$_2$.

The final value of the figure of merit for a suitable thermoelectric material should be at least 1 or higher. The thermal conductivity should be low enough, and the electrical conductivity should be high enough to meet this requirement. Temperature and charge carrier concentration also affect the value of the figure of merit (ZT), so we should carefully select the temperature and carrier concentration values for the optimum ZT value.[51] It is important to remember that the chemical potential controls the compound's carrier concen-

tration in the rigid band shift model. When n-type doping occurs, the Fermi level changes upward, which is consistent with a positive E$_f$, but when p-type doping occurs, the Fermi level shifts downward, which is consistent with a negative E$_f$.[56] The Seebeck coefficient and electrical conductivity have an opposite tendency with the carrier concentration, thus it is not as straightforward as we imagine that increasing the carrier concentration will likewise increase the value of ZT. It is always true that an ideal value of ZT for a specific material is

established under ideal circumstances because as the carrier concentration increases, the electrical conductivity increases, while the Seebeck coefficient declines.[53]

In the current study, SrO_x [$x = 1, 2$] with the aforementioned phases was investigated at temperatures between 300 and 1200 K with charge carrier concentrations of $\pm 10^{16}$, $\pm 10^{18}$, and $\pm 10^{20}$ cm^{-3}. According to Figure 9a,b, electrical conductivity values for all phases of SrO increase up to 500 K temperature before decreasing as temperature increases after that. For n-type hexagonal-1 phase SrO, higher electrical conductivity is discovered at a temperature of 500 K. In the case of SrO_2, the tetragonal material comparatively performs well in the n-type region and exhibits a significant electrical conductivity at room temperature, which also decreases with increasing temperature. Here, Figure 9a,b shows that the relationship between conductivity and temperature is not a straight line because as temperature increases, more electrons are excited from the valence band to the conduction band, and the conductivity of intrinsic semiconductors initially increases with temperature. After a certain threshold, however, the conductivity of the material begins to decrease, increasing the effects of charge carrier scattering due to high mobility and oscillations of atoms. It is said that a semiconductor's thermal conductivity typically increases as the temperature does. This is due to the fact that the phonons are able to move more freely and efficiently transmit heat, thanks to the stronger vibrations. In SrO_x [$x = 1, 2$], a tendency for thermal conductivity to fluctuate with temperature has been noted, as discussed above. Comparatively high values of thermal conductivity can be observed in n-type hexagonal-1 SrO and n-type tetragonal SrO_2 (Figure 9c,d).

As discussed, the Seebeck coefficient decreases with increasing charge carrier concentration as electrons fill all available positions and the Fermi level increases to the conduction band. As per Figure 10a–c, we have observed that the Seebeck coefficient of the material generally increases with increasing temperature at lower temperatures. This is due to the fact that the material's charge carriers are not excited enough to generate a sufficient amount of electrical potential at low temperatures, resulting in a low Seebeck coefficient. As the temperature increases, charge carriers gain more thermal energy, their mobility increases, and the Seebeck coefficient increases. As per Figure 10a–c, we also observe that at a high temperature, the Seebeck coefficient saturates; the reason behind this is that at a high temperature, the concentration of charge carriers becomes saturated, which means there are no more charge carriers left, so the value of the Seebeck coefficient does not increase. According to Figure 10, FCC phase SrO has a higher Seebeck coefficient than BCC phase SrO for n-type and p-type carrier concentrations, while in other cases, the Seebeck coefficient values have different behaviors for n-type and p-type. According to the ZT plot, all SrO phases with n-type concentration perform better than p-type; however, p-type concentration is crucial for orthorhombic SrO_2 to function well as a thermoelectric material due to the availability of more density of states in the valence region than the conduction region for orthorhombic SrO_2 (Table 6).

Dynamical Stability. The phonon dispersion curve is a useful tool for determining a crystalline material's stability. According to the harmonic approximation, a stable crystal should have positive phonon frequencies across the Brillouin zone. Any part of the dispersion curve with negative frequencies indicates that the crystal is dynamically unstable

in that direction. This is due to the fact that a negative frequency represents a nonrestorative restoring force, which moves the atoms further from their equilibrium position. Consequently, if it has a negative phonon frequency, the crystal will spontaneously deform in the direction of the phonon mode. A phase transition or even a collapse of the crystal structure can also be caused by this distortion.[57] Here, the dynamical stability at 0 GPa has been examined using phonon dispersion curves for the materials indicated above (Figure 11).[58]

In contrast to the BCC phase of SrO and all phases of SrO_2, which show negative frequencies in the figure, SrO with FCC(a), hexagonal-1(c), and hexagonal-2(d) display phonon curves only for positive frequencies, showing that these materials are dynamically stable at 0 GPa. We can readily confirm that the SrO-BCC, SrO_2-tetragonal, and SrO_2-orthorhombic phonon dispersion curves have negative frequencies from the preceding figure. Because they are high-pressure and -temperature phases, first-principles calculations typically cannot account for pressure and temperature since they only function at 0 GPa. So, these are not always dynamically unstable at all pressures just because they have such negative frequencies at 0 GPa.[59] Therefore, we decided to check the stability in terms of formation energy and we found that all of the phases show negative formation energy, which leads to a stable state of the material in terms of energy (Figure 12).[60]
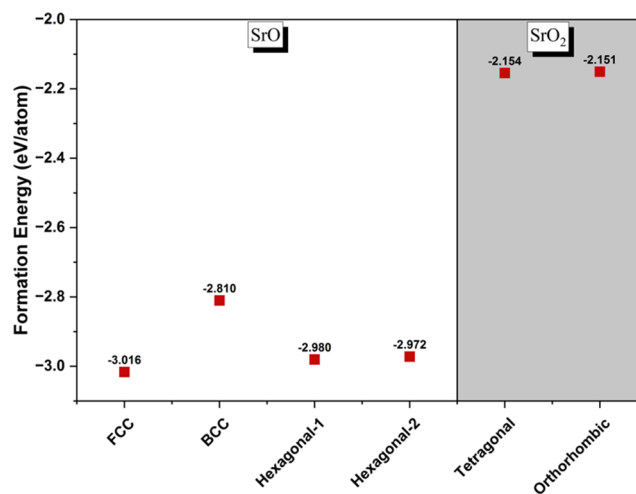

Figure 12. Formation energies (eV/atom) of various phases of SrO and SrO_2.

CONCLUSIONS

We conclude that the density of SrO_x [$x = 1, 2$] varies between 4.2 and 5.6 g/cm^3 because the oxygen ions are attracted toward each other through ionic bonding of the oxide, so with the increase in the number of "O", the density of "SrO" is observed to decrease. As far as the band gap is concerned, there is a net reduction in the energy band gap when the amount of oxygen in "SrO" increases. This decrease is the result of an increase in the number of energy levels in the "conduction band," which is brought on by oxygen atom electrons participating in the conduction region to a larger extent. With more oxygen present in "SrO", the energy band gap decreases from 3.30 to 2.27 eV. According to our findings, only the hexagonal phases

of SrO exhibit direct wide energy band gaps, whereas other phases of SrO_x $[x = 1, 2]$ only exhibit indirect wide energy band gaps. This indicates that optoelectronic applications like ultraviolet (UV) emission devices or LASER diodes are better suited for the hexagonal phases of SrO. The modest and indirect band gaps of the other SrO_x $[x = 1, 2]$ imply that they can be utilized as UV sensors or absorbers. All SrO_x $[x = 1, 2]$ materials have refractive indices that cross 2 in the ultraviolet range, making them effective ultraviolet light absorbers. All SrO_x $[x = 1, 2]$ phases have a first substantial absorption peak at about 50 nm (in the UV−C region), which is a wavelength that is difficult for other materials to absorb. SrO_x $[x = 1, 2]$ materials are, therefore, advantageous possibilities for UV sensors or absorbers. The FCC phases of SrO and the tetragonal phase of SrO_2 have good heat capacity and high Debye temperatures and have superior thermodynamic stability exhibiting strong bonding, high melting temperatures, high thermal conductivity, and high hardness. However, the said materials are unsuitable for thermoelectric devices with a 10^{16} cm^{-3} carrier concentration. This indicates that more investigation is required to optimize these materials' thermoelectric capabilities for certain applications. According to our overall findings, SrO and SrO_2 appear to be promising materials for a range of optoelectronic and thermoelectric applications. To completely comprehend these materials' characteristics and create novel devices based on them, more study is required. In addition to the above, note that that the study's findings are important since they offer fresh perspectives on the characteristics of SrO and SrO_2.

■ AUTHOR INFORMATION

Corresponding Author

Aditya M. Vora − *Department of Physics, University School of Sciences, Gujarat University, Ahmedabad 380 009 Gujarat, India;* ⊙ orcid.org/0000-0002-2520-0266; Email: voraam@gmail.com

Authors

Hiren S. Patel − *Department of Physics, University School of Sciences, Gujarat University, Ahmedabad 380 009 Gujarat, India;* ⊙ orcid.org/0000-0001-6760-4448

Vishnu A. Dabhi − *Department of Physics, University School of Sciences, Gujarat University, Ahmedabad 380 009 Gujarat, India;* ⊙ orcid.org/0000-0002-9841-6682

Complete contact information is available at:
https://pubs.acs.org/10.1021/acsomega.3c06221

Notes

The authors declare no competing financial interest.

■ ACKNOWLEDGMENTS

■ REFERENCES

(1) Hersam, M. C.; Jonas, D. A. *Strontium Oxide: Properties, Production, and Applications*; Springer, 2010.

(2) Hou, X. Y.; Tan, J.; Hu, C. E.; Chen, X. R.; Geng, H. Y. Thermoelectric Properties of Strontium Oxide under Pressure: First-Principles Study. *Phys. Lett. A* **2021**, *390*, No. 127083.

(3) Rajput, K.; Roy, D. R. Structure, Stability, Electronic and Thermoelectric Properties of Strontium Chalcogenides. *Phys. E* **2020**, *119* (October 2019), No. 113965.

(4) Cinthia, A. J.; Priyanga, G. S.; Rajeswarapalanichamy, R.; Iyakutti, K. Structural, Electronic and Mechanical Properties of Alkaline Earth Metal Oxides MO (M = Be, Mg, Ca, Sr, Ba). *J. Phys. Chem. Solids* **2015**, *79*, 23−42.

(5) Jain, A.; Ong, S. P.; Hautier, G.; Chen, W.; Richards, W. D.; Dacek, S.; Cholia, S.; Gunter, D.; Skinner, D.; Ceder, G.; Persson, Ka. Commentary: The Materials Project: A Materials Genome Approach to Accelerating Materials Innovation. *APL Mater.* **2013**, *1* (1), 11002.

(6) The Materials Project. Materials Data on SrO (Mp-2472) by Materials Project. DOI: 10.17188/1183681.

(7) Strauch, D.Semiconductors, New Data and Updates for IIa-VI Compounds with Mg and Sr (Structural Properties, Thermal and Thermodynamic Properties, and Lattice Properties). 2017 DOI: 10.1007/978-3-662-53620-9.

(8) The Materials Project. Materials Data on SrO (Mp-1009819) by Materials Project. DOI: 10.17188/1326302.

(9) Ganose, A. M.; Jain, A. Robocrystallographer: Automated Crystal Structure Text Descriptions and Analysis. *MRS Commun.* **2019**, *9* (3), 874−881.

(10) The Materials Project. Materials Data on SrO (Mp-754824) by Materials Project. DOI: 10.17188/1289589.

(11) Bernal, J. D.; Djatlowa, E.; Kasarnowsky, I.; Reichstein, S.; Ward, A. G. The Structure of Strontium and Barium Peroxides SrO2 and BaO2. *Z. Kristallogr. - Cryst. Mater.* **1935**, *92* (1−6), 344−354.

(12) The Materials Project. Materials Data on SrO (Mp-754282) by Materials Project. DOI: 10.17188/1289328.

(13) Ong, S. P.; Cholia, S.; Jain, A.; Brafman, M.; Gunter, D.; Ceder, G.; Persson, K. A. The Materials Application Programming Interface (API): A Simple, Flexible and Efficient API for Materials Data Based on REpresentational State Transfer (REST) Principles. *Comput. Mater. Sci.* **2015**, *97*, 209−215.

(14) The Materials Project. Materials Data on SrO2 by Materials Project. DOI: 10.17188/1201270.

(15) Abdus Salam, M. M. First Principles Study of Structural, Elastic and Electronic Structural Properties of Strontium Chalcogenides. *Chin. J. Phys.* **2018**, *57*, 418−434.

(16) Jacobson, J. L.; Nixon, E. R. Infrared Dielectric Response and Lattice Vibrations of Calcium and Strontium Oxides. *J. Phys. Chem. Solids* **1968**, *29* (6), 967−976.

(17) Souadkia, M.; Bennecer, B.; Kalarasse, F. Ab Initio Lattice Dynamics and Thermodynamic Properties of SrO under Pressure. *J. Phys. Chem. Solids* **2012**, *73* (1), 129−135.

(18) Wang, Y.; Wang, S.; Zhang, Y.; Lv, J.; Chen, Y.; Zheng, W.; ma, Y. Ground-State Crystal Structure of Strontium Peroxide Predicted from First Principles. *Inorg. Chem.* **2017**, *56*, 7545.

(19) Parr, R. G.; Yang, W. Density-Functional Theory of the Electronic Structure of Molecules. *Annu. Rev. Phys. Chem.* **1995**, *46* (1), 701−728.

(20) Kohn, W.; Becke, A. D.; Parr, R. G. Density Functional Theory of Electronic Structure. *J. Phys. Chem. A* **1996**, *100* (31), 12974−12980.

(21) Patel, H. S.; Dabhi, V. A.; Vora, A. M. Elastic Constants of Beryllium Oxide: A First-Principles Investigation. *AIP Conf. Proc.* **2020**, *2224*, No. 030006.

(22) Giannozzi, P.; Baroni, S.; Bonini, N.; Calandra, M.; Car, R.; Cavazzoni, C.; Ceresoli, D.; Chiarotti, G. L.; Cococcioni, M.; Dabo, I.; Dal Corso, A.; De Gironcoli, S.; Fabris, S.; Fratesi, G.; Gebauer, R.; Gerstmann, U.; Gougoussis, C.; Kokalj, A.; Lazzeri, M.; Martin-Samos, L.; Marzari, N.; Mauri, F.; Mazzarello, R.; Paolini, S.; Pasquarello, A.; Paulatto, L.; Sbraccia, C.; Scandolo, S.; Sclauzero, G.; Seitsonen, A. P.; Smogunov, A.; Umari, P.; Wentzcovitch, R. M. QUANTUM ESPRESSO: A Modular and Open-Source Software

Project for Quantum Simulations of Materials. *J. Phys.: Condens. Matter* **2009**, *21* (39), No. 395502.

(23) Giannozzi, P.; Andreussi, O.; Brumme, T.; Bunau, O.; Nardelli, M. B.; Calandra, M.; Car, R.; Cavazzoni, C.; Ceresoli, D.; Cococcioni, M.; Colonna, N.; Carnimeo, I.; Corso, A. D.; de Gironcoli, S.; Delugas, P.; Jr, R. A. D.; Ferretti, A.; Floris, A.; Fratesi, G.; Fugallo, G.; Gebauer, R.; Gerstmann, U.; Giustino, F.; Gorni, T.; Jia, J.; Kawamura, M.; Ko, H.-Y.; Kokalj, A.; Kucukbenli, E.; Lazzeri, M.; Marsili, M.; Marzari, N.; Mauri, F.; Nguyen, N. L.; Nguyen, H.-V.; Otero-de-la-Roza, A.; Paulatto, L.; Ponc, S.; Rocca, D.; Sabatini, R.; Santra, B.; Schlipf, M.; Seitsonen, A. P.; Smogunov, A.; Timrov, I.; Thonhauser, T.; Umari, P.; Vast, N.; Wu, X.; Baroni, S. Advanced Capabilities for Materials Modelling with QUANTUM ESPRESSO. *J. Phys.: Condens. Matter* **2017**, *29* (46), No. 465901.

(24) Malica, C.; Corso, A. Quasi-Harmonic Thermoelasticity of Palladium, Platinum, Copper, and Gold from First Principles. *J. Phys.: Condens. Matter* **2021**, *33*, No. 475901.

(25) Schlipf, M.; Gygi, F. Optimization Algorithm for the Generation of ONCV Pseudopotentials. *Comput. Phys. Commun.* **2015**, *196*, 36–44.

(26) Perdew, J. P.; Burke, K.; Ernzerhof, M. Generalized Gradient Approximation Made Simple. *Phys. Rev. Lett.* **1996**, *77* (18), 3865.

(27) Hamann, D. R. Optimized Norm-Conserving Vanderbilt Pseudopotentials. *Phys. Rev. B* **2013**, *88* (8), No. 085117.

(28) Quantum-Simulation.Org. www.quantum-simulation.org. 2023. http://www.quantum-simulation.org/potentials/sg15_oncv/.

(29) Patel, H. S.; Dabhi, V. A.; Vora, A. M. Adverse Effect of K-Mesh Shifting in Several Crystal Systems: An Analytical Study. *Mater. Today Proc.* **2022**, *57*, 275.

(30) Wang, Y.; Lv, J.; Zhu, L.; Ma, Y. CALYPSO: A Method for Crystal Structure Prediction. *Comput. Phys. Commun.* **2012**, *183* (10), 2063–2070.

(31) Königstein, M.; Sokol, A. A.; Catlow, C. R. A. Electronic Structure and Bonding in Crystalline Peroxides. *Phys. Rev. B* **1999**, *60*, 4594–4604.

(32) Dresselhaus, M.; Dresselhaus, G.; Cronin, S. B.; Gomes, A. *Solid State Properties*; Springer, 2018.

(33) Madsen, G. K. H.; Singh, D. J. BoltzTraP. A Code for Calculating Band-Structure Dependent Quantities. *Comput. Phys. Commun.* **2006**, *175* (1), 67–71.

(34) Kalpana, G.; Palanivel, B.; Rajagopalan, M. Electronic and Structural Properties of Alkaline-Earth Oxides under High Pressure. *Phys. Rev. B* **1995**, *52* (1), 4–7.

(35) Azam, S.; Irfan, M.; Abbas, Z.; Rani, M.; Saleem, T.; Younus, A.; Akhtar, N.; Liaqat, B.; Shabbir, M. Z.; Al-Sehemi, A. G. DFT Study of the Electronic and Optical Properties of Ternary Chalcogenides AlX$_2$Te$_4$. *Mater. Res. Express* **2019**, *6* (11), No. 116314.

(36) Kumar, A.; Jharwal, S. M.; Prajapati, B.; Kumar, M.; Singh, V.; Singh, R. P. Theoretical Investigations on Electronic and Optical Properties of Half Heusler Alloy,FeNbSb for Opto-Electronic Applications. *Opt. Quantum Electron.* **2022**, *54*, No. 717.

(37) Dresselhaus, M. SOLID STATE PHYSICS PART II Optical Properties of Solids. http://web.mit.edu/6.732/www/6.732-pt2.pdf (accessed 2022–07–18).

(38) Fox, A. M. *Optical Properties of Solids*; Oxford University Press, 2012.

(39) Ghebouli, M. A.; Ghebouli, B.; Bouhemadou, A.; Fatmi, M.; Bouamama, K. Structural, Electronic, Optical and Thermodynamic Properties of SrxCa1−xO, BaxSr1−xO and BaxCa1−xO Alloys. *J. Alloys Compd.* **2011**, *509*, 1440–1447.

(40) Marzari, N.; Singh, D. J. Ab Initio Determination of the Dielectric Response of GaAs, AlAs, C, and SrO in the Weighted-Density Approximation. *J. Phys. Chem. Solids* **2000**, *61*, 321–325.

(41) Duan, Y.; Qin, L. Q.; Tang, G. Y.; Shi, L. First-Principles Study of Ground- and Metastable-State Properties of XO (X = Be, Mg, Ca, Sr, Ba, Zn and Cd). *Eur. Phys. J. B* **2008**, *66*, 201–209.

(42) Penn, D. R. Wave-Number-Dependent Dielectric Function of Semiconductors. *Phys. Rev. J. Arch.* **1962**, *128* (5), 2093–2097.

(43) Soussi, A.; Elfanaoui, A.; hssi, A. A.; Taoufiq, M.; Asbayou, A.; Boulkaddat, L.; Labchir, N.; Markazi, R.; Ihlal, A.; Bouabid, K. Morphological, Structural, Electronic and Optical Properties of Deposited 4d-Mo Doped TiO2 Thin Films Compared to First-Principles Calculations. *Mater. Today Commun.* **2023**, *36*, No. 106520.

(44) Pynchon, G. E.; Sieckmann, E. F. Refractive Index of Strontium Oxide. *Phys. Rev. J. Arch.* **1966**, *143* (2), 595–597.

(45) Dadsetani, M.; Beiranvand, R. Optical Properties of Alkaline-Earth Metal Oxides from First Principles. *Solid State Sci.* **2009**, *11*, 2099–2105.

(46) Lukačević, I. High Pressure Lattice Dynamics, Dielectric and Thermodynamic Properties of SrO. *Phys. B Condens. Matter* **2011**, *406*, 3410–3416.

(47) Ivanovskii, A. L.; Shein, I. R.; Makurin, Y. N.; Kiiko, V. S.; Gorbunova, M. A.; Mouhat, F.; Coudert, F. X.; Dal Corso, A. Theoretical Study of Phonon Dispersion, Elastic, Mechanical and Thermodynamic Properties of Barium Chalcogenides. *Int. J. Modern Phys. B* **2009**, *32* (8), No. 1850092.

(48) Barin, I. *Thermochemical Data of Pure Substances*; Vch Verlagsgesellschaft, 1995.

(49) Gmelin, E. Thermal Properties of Alkaline-Earth-Oxides I. Specific Heat Measurements 1–3 Centre National De Recherches Sur Les Tres Basses Temperatures. *Zeitschrift für Naturforschung A* **1969**, *24*, 1794–1800.

(50) Jones, L. E.; Liebermann, R. C. Elastic and Thermal Properties of Fluoride and Oxide Analogues in the Rocksalt, Fluorite, Rutile and Perovskite Structures. *Phys. Earth Planet. Inter.* **1974**, *9*, 101–107.

(51) Salik, L.; Bouhemadou, A.; Boudiaf, K.; Saoud, F. S.; Bin-Omran, S.; Khenata, R.; Al-Douri, Y.; Reshak, A. H. Structural, Elastic, Electronic, Magnetic, Optical, and Thermoelectric Properties of the Diamond-like Quaternary Semiconductor CuMn2InSe4. *J. Supercond. Nov. Magn.* **2020**, *33* (4), 1091–1102.

(52) Nemir, D.; Beck, J. On the Significance of the Thermoelectric Figure of Merit Z. *J. Electron. Mater.* **2010**, *39* (9), 1897–1901.

(53) Kang, C.; Wang, H.; Bahk, J.-H.; Kim, W. *Thermoelectric Materials and Devices*; The Royal Society of Chemistry, 2015, pp 107–141. DOI: 10.13140/2.1.1533.0087.

(54) Scheidemantel, T. J.; Draxl, C.; Thonhauser, T.; Badding, J. V.; Sofo, J. O. Transport Coefficients from First-Principles Calculations. *Phys. Rev. B* **2003**, *68* (12), No. 125210.

(55) Hnuna, L.; Haidar, E.; Djamel, B.; Stampfl, C.; Mohammed, S.; Pachuau, Z. First-principles Study of Optical and Thermoelectric Properties of Zn$_3$As$_2$ and ZnSb. *Nano Sel.* **2023**, *4*, 551.

(56) Zou, D. F.; Xie, S.; Liu, Y. Y.; Lin, J.; Li, J. Y. Electronic Structure and Thermoelectric Properties of Half-Heusler Zr0.5Hf0.5NiSn by First-Principles Calculations. *J. Appl. Phys.* **2013**, *113* (19), No. 193705.

(57) Parlinski, K. Lattice Dynamics: Vibrational Modes. In *Encyclopedia of Condensed Matter Physics*; Bassani, F.; Liedl, G. L.; Wyder, P., Eds.; Elsevier: Oxford, 2005; pp 98–102. DOI: 10.1016/B0-12-369401-9/00509-X.

(58) Wang, X.-T.; Yang, T.; Cheng, Z.; Surucu, G.; Wang, J.; Zhou, F.; Zhang, Z.; Zhang, G. Topological Nodal Line Phonons: Recent Advances in Materials Realization. *Appl. Phys. Rev.* **2022**, *9* (4), No. 41304.

(59) Cao, W.; Wang, Z.; Miao, L.; Shi, J.; Xiong, R. Thermoelectric Properties of Strained β-Cu$_2$Se. *ACS Appl. Mater. Interfaces* **2021**, *13* (29), 34367–34373.

(60) Guo, S.; Liu, Z.; Feng, Z.; Jia, T.; Anand, S.; Snyder, G. J.; Zhang, Y. Prediction of Improved Thermoelectric Performance by Ordering in Double Half-Heusler Materials. *J. Mater. Chem. A* **2020**, *8* (44), 23590–23598.